Journal of Energy Chemistry 100 (2025) 693–701

Contents lists available at ScienceDirect

Journal of Energy Chemistry

journal homepage: www.elsevier.com/locate/jechem

http://www.journals.elsevier.com/journal-of-energy-chemistry/

Dielectric-ion-conductive $ZnNb_2O_6$ layer enabling rapid desolvation and diffusion for dendrite-free Zn metal batteries

Haifeng Yang [a,b], Jian Wang [c,e,*], Panpan Zhang [a], Xiaomin Cheng [b], Qinghua Guan [b], Jing Dong [b], Bixian Chen [a,b], Lujie Jia [b], Jing Zhang [d], Yongzheng Zhang [f], Yunjian Liu [a,*], Hongzhen Lin [b,*]

[a] School of Materials Science and Engineering, Jiangsu University, Zhenjiang 212013, Jiangsu, China
[b] i-Lab & CAS Key Laboratory of Nanophotonic Materials and Devices, Suzhou Institute of Nano-Tech and Nano-Bionics, Chinese Academy of Sciences, Suzhou 215123, Jiangsu, China
[c] Helmholtz Institute Ulm (HIU), Ulm D89081, Germany
[d] School of Materials Science and Engineering, Xi'an University of Technology, Xi'an 710048, Shaanxi, China
[e] Karlsruhe Institute of Technology (KIT), Karlsruhe D76021, Germany
[f] State Key Laboratory of Chemical Engineering, East China University of Science and Technology, Shanghai 200237, China

ARTICLE INFO

Article history:
Received 24 August 2024
Revised 9 September 2024
Accepted 9 September 2024
Available online 16 September 2024

Keywords:
Zn metal battery
Dielectric artificial layer
Rapid ion diffusion
Zincophilic diffusion
Active water inhibition

ABSTRACT

Rechargeable aqueous zinc-metal batteries (AZMBs) are promising candidates for large-scale energy storage systems due to their low cost and high safety. However, their performance and sustainability are significantly hindered by the sluggish desolvation kinetics at the electrode/electrolyte interface and the corresponding hydrogen evolution reaction where active water molecules tightly participate in the Zn $(H_2O)_6^{2+}$ solvation shell. Herein, learnt from self-generated solid electrolyte interphase (SEI) in anodes, the dielectric but ion-conductive zinc niobate nanoparticles artificial layer is constructed on metallic Zn surface (ZNB@Zn), acting as a rapid desolvation promotor. The zincophilic and dielectric-conductive properties of ZNB layer accelerate interfacial desolvation/diffusion and suppress surface corrosion or dendrite formation, achieving uniform Zn plating/stripping behavior, as confirmed by electronic/optical microscopies and interface spectroscopical measurements together with theoretical calculations. Consequently, the as-prepared ZNB@Zn electrode exhibits excellent cycling stability of over 2000 h and robust reversibility (99.54%) even under high current density and depth of discharge conditions. Meanwhile, the assembled ZNB@Zn-based full cell displays high capacity-retention rate of 80.21% after 3000 cycles at 5 A g^{-1} and outstanding rate performance up to 10 A g^{-1}. The large-areal pouch cell is stabilized for hundreds of cycles, highlighting the bright prospects of the dielectric but ion-conductive layer in further application of AZMBs.

1. Introduction

As non-renewable fossil fuels depleted, intense needs of energy storage systems for periodic clean energy sources, such as solar, wind, and tidal energy, have become increasingly urgent [1–4]. Rechargeable aqueous zinc metal batteries (AZMBs) have garnered significant interests in recent years due to the high theoretical specific capacity (820 mA h g^{-1}, 5855 mA h cm^{-3}) and the appropriate redox potential (−0.76 V vs. SHE) of Zn metal anode [5–8]. However, Zn corrosion and hydrogen evolution reaction (HER) resulted from $[Zn(H_2O)_6]^{2+}$ solvation shell lead to undesirable Coulombic efficiency (CE) and Zn dendrites formation produced by non-uniform ion flux, seriously reducing the battery's lifespan and severely impeding the commercial viability of AZMBs [9–11].

To date, efforts to decrease high desolvation barrier of $[Zn(H_2O)_6]^{2+}$ clusters focus on electrolyte engineering or optimal solid electrolyte interphase (SEI) construction at the electrode/electrolyte interface for modulating Zn^{2+} flux [12–15]. Electrolyte engineering is centering on modifying and modulating the compositions of aqueous electrolyte to adjust the Zn^{2+} coordination environment [16–20]. However, these modulations always compromise the original ionic conductivity of the aqueous electrolytes, inevitably leading to the blockage of Zn^{2+} transport and incurring high costs. Alternatively, the artificial SEI layers such as organic interface layers [21–24], inorganic protective layers [25–28], and alloy-induced layers are constructed [29–31]. In the original electrochemically-generated SEI composite, the self-generated SEI is composed of the electron-insulative but

* Corresponding authors.
E-mail addresses: jian.wang@kit.edu, wangjian2014@sinano.ac.cn (J. Wang), lyjian122331@ujs.edu.cn (Y. Liu), hzlin2010@sinano.ac.cn (H. Lin).

https://doi.org/10.1016/j.jechem.2024.09.010

ion-conductive substances such as ZnF_2. Especially, the SEI is beneficial for Zn ion conductivity and prevents electron contact without the formation of HER. The SEI could also regulate the nucleation process of Zn^{2+}, guide uniform deposition, or isolate active water to inhibit side reactions [32–34]. However, most designs lack satisfactory Zn ion transport kinetics across the artificial layers, which burdens and costs extra energy. Simultaneously, the Zn deposition process includes the steps of adsorption, desolvation, and diffusive migration, which can not be further modulated via current layer constructions [35]. Therefore, designing a multifunctional artificial SEI layer that regulates the Zn^{2+}/Zn^0 diffusion still remains a great of challenge.

As known, the side reactions of HER and surface corrosion are also related to the interfacial conductivity with electron injection and solvation shell behaviors of active water molecules, deteriorating the performance and lifespan of AZMBs [36]. Decreasing the ratio of active water from the $[Zn(H_2O)_6]^{2+}$ solvation shell is desired for the inhibition of HER. For example, modulating the active water ratio in the inner Helmholtz plane (IHP) layer by introducing organic solvents in the electrolyte does reduce the occurrence of surface corrosion as well. Meanwhile, blocking the electrons with active water molecules via interface design seems more effective towards the inhibition of HER. For instance, ZnF_2 is widely reported to separate the electronic conductivity between electrode and active materials [37]. However, the Zn ion transport in ZnF_2 remains weak and the dendrite is still formed after several cycles. Therefore, constructing the dielectric but ion-conductive artificial layer is of significance for fast ion desolvation and atom diffusion toward dendrite-free plating morphology [38–41].

Herein, the dielectric but ion-conductive zinc niobate (ZNB) nanoparticle layer is constructed as an artificial SEI layer on Zn anode surface (named as ZNB@Zn), providing fast transport pathways for sieving solvated ions and thus enhancing the desolvation and transport kinetics for Zn plating process. Specifically, $[Zn(H_2O)_6]^{2+}$ clusters are initially adsorbed on the ZNB layer, undergo electrostatic forces and microporous sieving, and strip the solvent shell, allowing them to easily pass through the SEI layer. Both experimental results of electrochemistry and spectroscopies and theoretical calculations show that fast-conducting channels and zincophilic properties of ZNB alter the solvation structure of Zn^{2+} at the electrode/electrolyte interface, reduce transport resistance, and lead to fast desolvation behavior and uniform Zn deposition. As a result, the ZNB@Zn anode is capable of maintaining ultralow overpotential of 24.9 mV at 1 mA cm^{-2} and lasts for more than 2000 h with excellent cycle reversible efficiency of 99.54%. More impressively, the coupled full cell could operate for over 3000 cycles at 5 A g^{-1} with a high capacity-retention (80.21%) and the as-fabricated pouch cell is stabilized for hundreds of cycles with the areal capacity of 2 mA h cm^{-2}, validating promising practical application prospects for AZMBs.

2. Experimental

2.1. Synthesis of ZNB nanoparticles

0.1488 g of $Zn(NO_3)_2{\cdot}5H_2O$ and 0.1809 g of $C_{10}H_5NbO_{20}$ were dissolved in 200 mL of deionized water and then 1 M HCl was added dropwise until all solids were completely dissolved with continously stirring. A proper amout of ammonia was then added slowly to adjust pH to 8.5–9. After stirring for another 0.5 h, the resulting mixture was centrifuged to get the precipitate. Afterward, the collected solids were dried in an oven at 60 °C for 12 h and then calcined at 650 °C for 4 h under the dry air atmosphere with the heating rate of 5 °C min^{-1}. After cooling down to room temperature, $ZnNb_2O_6$ nanoparticles are achieved.

2.2. Preparation of ZNB@Zn anode

The ZNB powders was combined with polyvinylidene fluoride (PVDF) in a ratio of 9:1 and mixed with *N*-methyl-2-pyrrolidone (NMP) under stirring, creating a homogeneous slurry. This slurry was then coated on the polished Zn metal foil using a 50 μm scraper. And then, it was dried in an oven at 60 °C for 4 h to rule out all the solvents. Finally, the foils were cut to the desired sizes to obtain ZNB@Zn anodes.

2.3. Preparation of V_2O_{5-x} cathode

The fabrication of V_2O_{5-x} cathode is similar to our previous report [42]. Briefly, the commercial V_2O_5 was treated at 400 °C for 2 h under the 5% H_2/Ar atmosphere. The V_2O_{5-x} cathode was prepared by mixing V_2O_{5-x}, Super P, and PVDF in a ratio of 7:2:1 in NMP solvent to form homogeneous slurry. This slurry was coated onto a carbon film, which was then cut into appropriate sizes. The average areal mass loading of the active material was approximately 1 mg cm^{-2}.

3. Results and discussion

First of all, the ZNB ($ZnNb_2O_6$) nanoparticles were synthesized by co-precipitation method and then coated on the metallic Zn anode surface, forming an artificial SEI layer. As illustrated in Fig. 1(a), the ortho-octahedral NbO_6 in the ZNB is bridged with oxygen to form a negatively charged two-dimensional (2D) layered structure, in which the Zn atoms are compensated to be the pillars of the interlayer, leading to the formation of numerous transport paths with pore sizes around 3.2 Å, sieving the solvated $[Zn(H_2O)_6]^{2+}$ clusters and converting them to free Zn^{2+} and then quickly reaching the Zn anode surface for reduction and deposition [9,43]. In contrast, the exposed surface and retarded kinetics of the bare Zn anode lead to rampant corrosion and dendrite growth and the water molecules will be decomposed on the surface of pristine Zn, leaving the side reactions of HER and corrosion. The scanning electron microscope (SEM) images in Fig. 1(b) and Fig. S1 show that the as-synthesized ZNB particles are approximately 100 nm, and the homogeneous coating on the surface of Zn anode forms a dense coating layer with about 5 μm in thickness (Fig. 1c), which is suitable for maintaining rapid ion transport. The X-ray photoelectron spectroscopy (XPS) reveals that the Nb 3*d* spectrum (206.7 eV) shifts to lower binding energies compared to typical Nb_2O_5 (207.1 eV), while the Zn 2*p* spectrum (1021.4 eV) shifts to higher binding energies (Fig. 1d and Fig. S2), indicating the electron flow direction in the Zn-O-Nb system [43]. The X-ray diffraction (XRD) pattern in Fig. 1(e) displays the orthorhombic phase of $ZnNb_2O_6$, which is ascribed to JCPDS No.76-1827, confirming the successful synthesis of ZNB [44]. The N_2 adsorption and desorption isotherms with the corresponding pore size distributions analysis (Fig. S3) show that the pore size distribution of ZNB concentrates on ~3.09 nm and the homogeneous pore size distribution can effectively regulate the lateral diffusion of Zn^{2+} and ensure the homogeneous deposition at the interface.

The desolvation behaviors are witnessed by various spectroscopic measurements. The interface-sensitive in-situ sum-frequency generation (SFG) spectroscopy is used to probe water molecular information at electrode/electrolyte interface [45–48]. As depicted in Fig. S4, two laser beams (one visible and one infrared light) overlap at the interface and a SFG signal is generated and reflected. The apparent solvent peaks generated by the stretching vibration of O–H bonds in 3200–3500 cm^{-1} range can be observed. When a bias voltage is applied to the interface (Fig. 2a), the electric field causes the movement of solvated ions, monitoring the state of

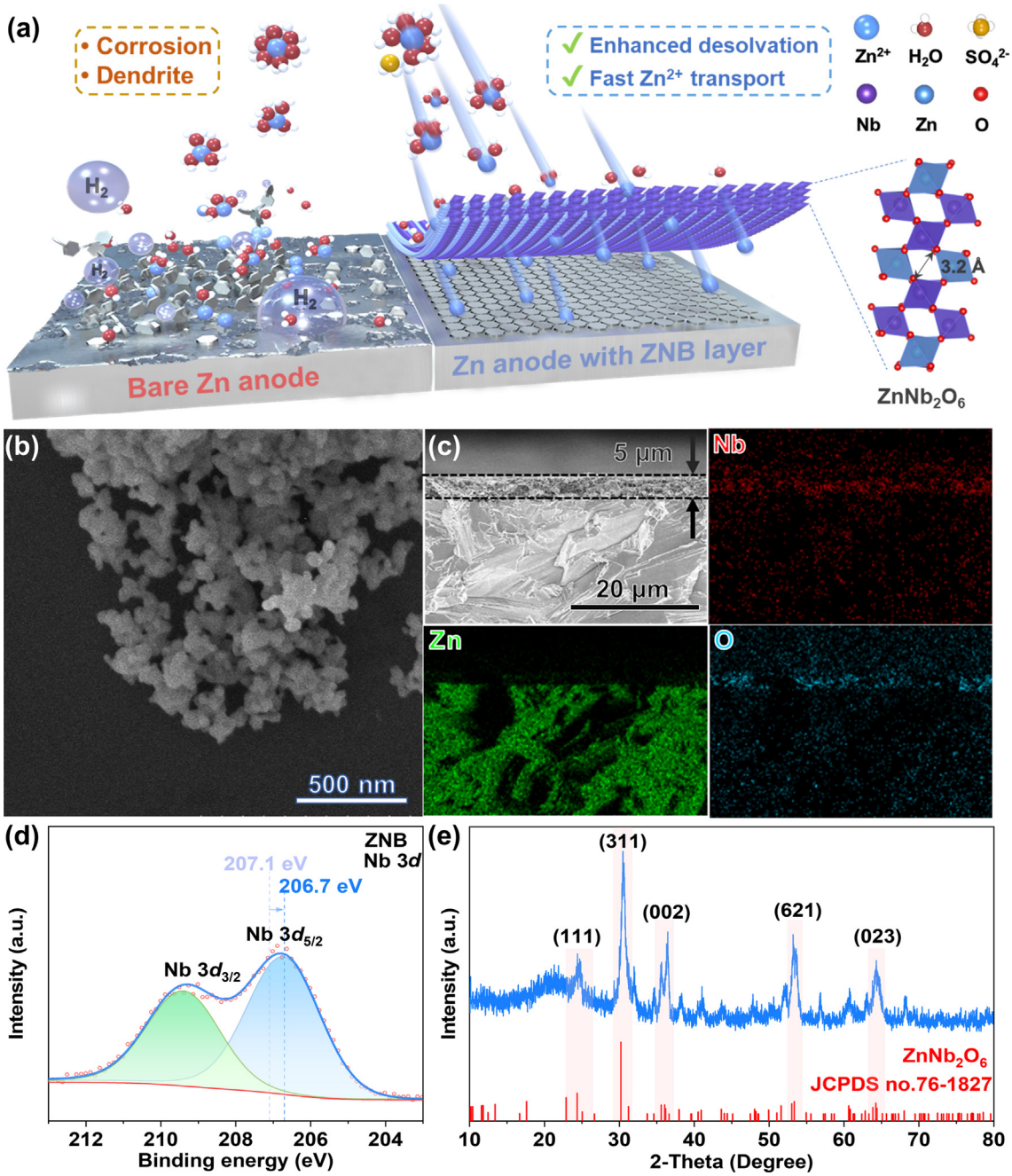

Fig. 1. (a) Schematic illustration of ZNB layer at electrode/electrolyte interface in dealing with desolvation/diffusion kinetics and potential side reaction. (b) SEM image of synthesized ZNB nanoparticle. (c) SEM image of ZNB layer on metallic Zn and corresponding elemental mappings. (d) The high-resolution XPS of Nb 3*d* spectrum. (e) XRD pattern of synthesized ZNB.

interface water molecules [48–51]. Notably, upon applying the bias voltage, the peak at 3280 cm^{-1}, attributed to strongly bound solvated water, experienced a substantial intensity drop for the ZNB@Zn/electrolyte interface in sharp contrast to the response of the bare Zn/electrolyte interface. Meanwhile, the reduced peak at 3450 cm^{-1} indicates weakly bound solvated water molecules in the solvation shell (Fig. 2b and c) [13]. This suggests that Zn^{2+} at the interface can more easily extract from the solvation sheath under the guidance of the ZNB layer, leading to faster interfacial kinetics. Further, Raman spectroscopy (Fig. 2d) also displays changes in the solvation structure, revealing a shift from solvent-separated ion pairs (SSIP, $[Zn^{2+}(H_2O)_6OSO_3^{2-}]$) to contact ion pairs (CIP, $[Zn^{2+}(H_2O)_5OSO_3^{2-}]$), increasing from 44.7% at the bare Zn/electrolyte interface to 67.7% at the ZNB@Zn/electrolyte interface, implying closer contact of $[Zn^{2+}SO_4^{2-}]$ ion pairs under the induction of ZNB [15,52,53].

Density functional theory (DFT) calculations explain the intrinsic driving force of the ZNB layer for accelerating desolvation by simulating the adsorption energy of Zn^{2+} on the bare or ZNB layer decorated surface (Fig. 2e) [54–58]. As known, in the electrolyte, the bare Zn^{2+} is always coordinated with water molecules and forms the $Zn(H_2O)_6^{2+}$ clusters, where the Zn^{2+} is located in the center of the solvation shell. At the electrode/electrolyte interface, the stronger binding ability can help Zn^{2+} to overcome the desolvation reaction barrier easily, driving the reaction forward and proceeding to the next transport process for leaving water in the solvation

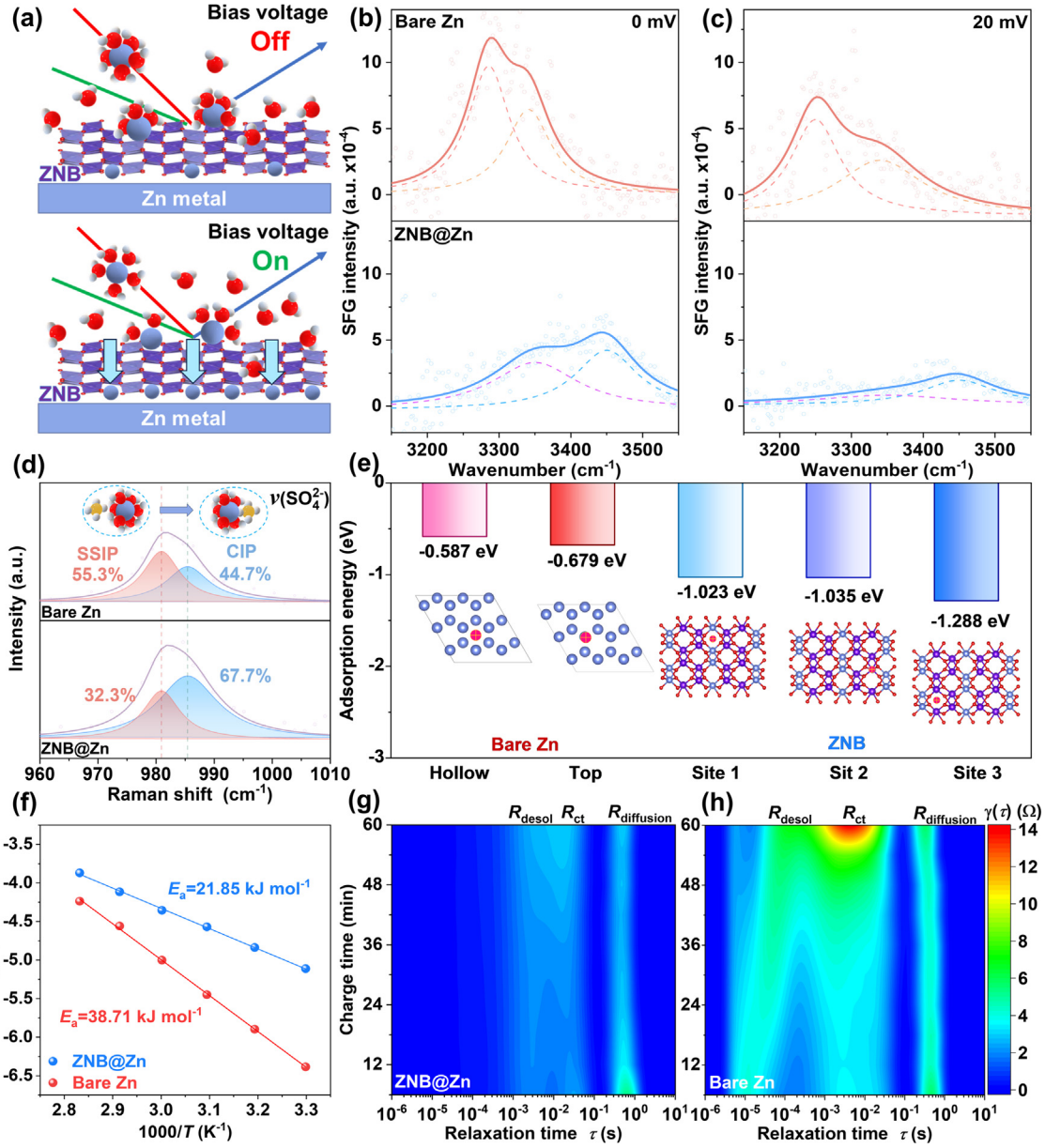

Fig. 2. (a) Schematic illustration evolution of $[Zn(H_2O)_6]^{2+}$ at the interface with electric field. (b, c) Changes of O–H SFG bond signal in bare Zn/electrolyte and ZNB@Zn/electrolyte interface with/without bias voltage. (d) Raman spectra of SO_4^{2-} on the bare Zn and ZNB@Zn surface. (e) Adsorption energy of Zn atom at different sites on the Zn (002) and ZNB (001) surface. (f) Desolvation activation energy from Arrhenius curve. DRT analysis of (g) ZNB@Zn and (h) bare Zn based symmetric cells during charging process.

shell structure. The adsorption energy on the ZNB layer surface (−1.288 eV) was higher than that on the bare Zn surface (−0.679 eV), indicating a stronger tendency for Zn^{2+} to be adsorbed on the ZNB surface, which helps water to escape from solvated shell structure to promote desolvation for bare Zn^{2+}. The electrochemical impedance spectroscopy (EIS) conducted at different temperatures depicts the activation energy (E_a) via the Arrhenius equation, which is often used to quantitatively describe the desolvation kinetics. It is clear that the ZNB@Zn anode surface exhibited a much lower E_a (21.86 kJ mol^{-1}) in comparison with the bare Zn (38.71 kJ mol^{-1}) (Fig. 2f and Fig. S5). The lower activation energy indicates a more easily facilitated desolvation process and reduced resistance of Zn^{2+} desolvation and diffusion. In-situ EIS and distribution relaxation times (DRT) analyses of symmetric cells charged over 60 min (Fig. 2g and h and Fig. S6) reveal three peaks [59–63], representing the three reaction control steps of desolvation, charge transfer, and diffusion, respectively [64–67]. The kinetics of ZNB@Zn anode demonstrates lower impedance and weak polarization, while the bare Zn metal anode severely hindered charge transfer process with a large polarization, verifying the significant improvement of the ZNB layer on the interfacial reaction kinetics.

Linear scanning voltammetry (LSV) tests show an extended electrochemical window from −70 to −98 mV and suppressed HER for the Zn anode protected by ZNB layer (Fig. 3a). The Tafel plot reveals a lower corrosion current (I_{corr}) for the ZNB@Zn anode (5.651 mA cm^{-2}) in comparison to bare Zn (6.758 mA cm^{-2}), suggesting improved corrosion resistance of the ZNB layer against interfacial active water molecules (Fig. 3b). The two peaks in the Raman spectrum at 3000–3800 cm^{-1}, caused by the stretching vibration of the O–H bond, indicate the ratio of bound water to free water (Fig. S7). Compared to 76.8% on the bare Zn surface, the active water content on the ZNB@Zn surface is reduced to 67.2%,

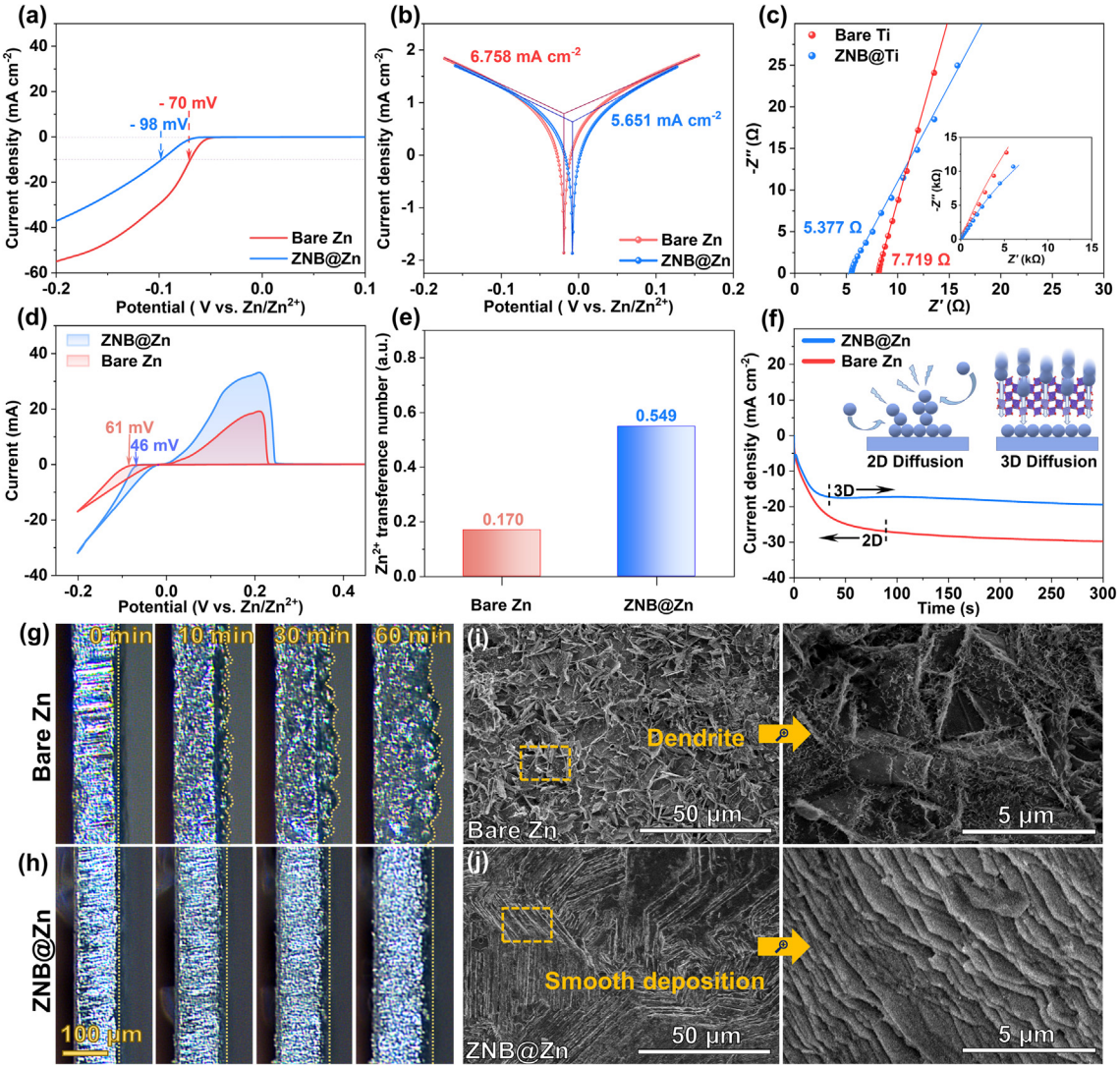

Fig. 3. (a) LSV testing of bare Zn//Ti and ZNB@Zn//Ti electrodes. (b) Tafel curves of bare Zn and ZNB@Zn electrodes. (c) Ohmic resistance of bare Ti and ZNB@Ti symmetric cell. (d) CV curves of bare Zn//Cu and ZNB@Zn//Cu. (e) Zn^{2+} transference number of bare Zn and ZNB@Zn symmetric cells. (f) Chronoamperometry curves of bare Zn and ZNB@Zn electrode. In-situ optical microscopy observation of the deposition evolution of (g) bare Zn and (h) ZNB@Zn anode at 3 mA cm^{-2}. SEM images showing the surface morphology of (i) bare Zn and (j) ZNB@Zn anode after 50 cycles at 1 mA cm^{-2}.

which demonstrates that the ZNB favors in inhibiting corrosion reactions of Zn anode [68]. The intrinsic Ohmic resistance (R_0) in the Ti symmetric cell with/without ZNB dielectric-conductive layer (Fig. 3c) reflects the ionic conductivity of the internal environment, and it can be seen that the battery system with ZNB layer has a lower R_0 than the one with bare Zn (5.38 vs. 7.72 Ω). Meanwhile, the cyclic voltammetry (CV) curve of ZNB@Zn//Cu half-cell shows a lower polarization of 46 mV (Fig. 3d), while a higher peak current indicates more nucleation sites and faster diffusion on the ZNB@Zn anode surface. The Zn^{2+} transference number (t^{2+}_{Zn}) of ZNB@Zn is calculated to be 0.549, which exceeds three times that of bare Zn (0.170) (Fig. 3e and Fig. S8), ensuring sufficient Zn ions for the subsequent diffusion and nucleation stages. Ultimately, the enhanced ion desolvation kinetics, sieving ion transport pathways, and dense active site distribution facilitate a fast and flat Zn deposition process on the ZNB@Zn anode. As depicted in Fig. 3(f), during the 2D diffusion stage, unconstrained Zn^{2+} exhibits concentrated diffusion and irregular nucleation due to the tip-discharge effect. However, under the influence of the ZNB layer, the Zn anode experiences a steady-state three-dimensional (3D) lateral diffusion stage much earlier. This early occurrence is crucial to mitigate the possible formation of dendrites and improve uniformity of Zn deposition, facilitating and promoting stable and uniform Zn plating behavior.

At the same time, the function of ZNB layer in dendrite inhibition is also observed by the in-situ optical microscopy images, revealing changes and evolutions of Zn surface morphology during the deposition process (Fig. 3g and h). After plating for 10 min, the randomly distributed granular bumps were generated on the metallic Zn surface. In contrast, the surface of ZNB@Zn maintained flat and dendrite-free deposition morphology due to rapid desolvation and efficient ion flux regulation. SEM images of the cycled Zn anode surfaces (Fig. 3i and j and Fig. S9) further confirm these observations. The bare Zn anode exhibited numerous randomly oriented dendrites in high- or low-resolution images [69]. Conversely, the ZNB@Zn anode displayed orderly dendrite-free deposition, confirming the positive effect of the ZNB layer on modulating deposition behavior and inhibiting the HER. This uniformity and stability highlight the potential of the ZNB layer in enhancing both the performance and longevity of Zn anodes in battery applications.

Thanks to the excellent zincophilicity and interfacial desolvation ability of the ZNB layer, the ZNB@Zn anode exhibited a significantly lower initial nucleation overpotential (38.7 mV, Fig. 4a), much lower than that on bare Zn (87.9 mV). The galvanostatic intermittent titration (GITT) test of a symmetric cell revealed that the fast ion transport paths in the ZNB layer reduce the concentration polarization from 8.37 to 4.34 mV (Fig. 4b and Fig. S10) [35,66]. This optimization of desolvation/deposition kinetics is further confirmed by EIS tests. After 50 cycles, the impedance of the ZNB@Zn symmetric cell was only 27.66 Ω, nearly one fourth of bare Zn (102.35 Ω) (Fig. 4c and Fig. S11). Thus, the ZNB@Zn symmetric cell demonstrated excellent rate performance, as shown in Fig. 4(d) and Fig. S12. When the current density was increased from 1 to 30 mA cm^{-2}, the ZNB@Zn cell maintained an ultra-low voltage hysteresis within 46 mV (133 mV for bare Zn). The difference even became more pronounced at higher current densities, reflecting enhanced interfacial ionic transport kinetics derived from the reduced desolvation barrier and diffusion resistance by ZNB layer. Further cycling at 1 mA cm^{-2} (Fig. 4e), the ZNB@Zn symmetric cell maintained an extraordinarily long-term life over 2000 h with a low voltage polarization of 24.9 mV. In contrast, the bare Zn electrode suffered from short circuit failure within a significantly shorter time of 120 h. Increasing to 5 mA cm^{-2} (Fig. S13), the cycle life (1500 h) of ZNB@Zn symmetric cell still far exceeded that of bare Zn anode based symmetric cell. It shows excellent cycling stability in comparison with recently reported Zn anode artificial layer (Fig. S14 and Table S1). In resting experiments (Fig. S15), the bare Zn symmetric cell failed due to the accumulation of by-products on the anode surface with extremely high polarization. Meanwhile, the ZNB@Zn symmetric cell remained stable after each 100 h interval, demonstrating the ability of ZNB layer to maintain a stable cycling process by corrosion prevention. Even under a depth of discharge (DOD) of 34.1% for 50 μm Zn foil (Fig. 4f), the ZNB layer on Zn anode significantly extended its life-

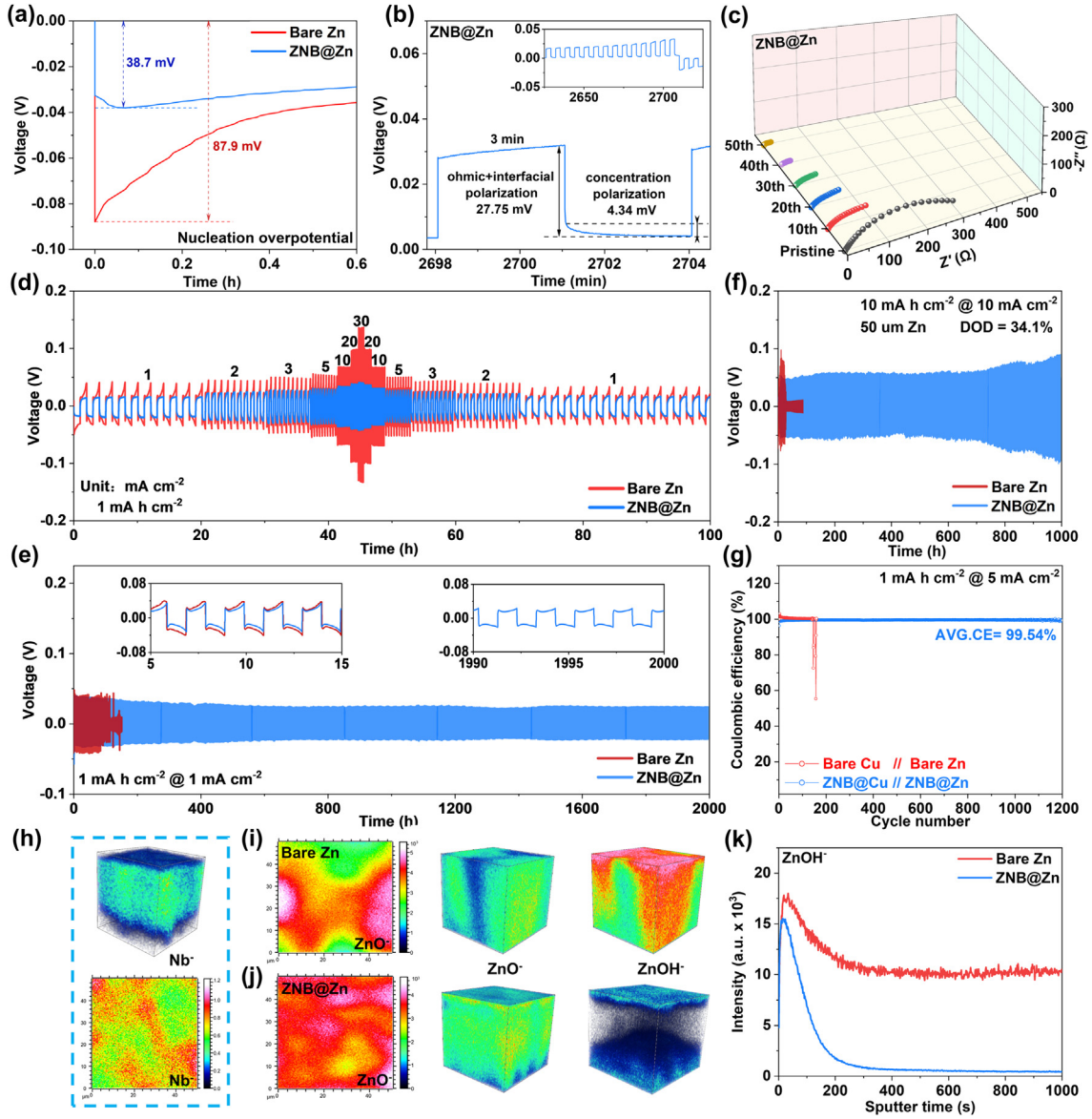

Fig. 4. (a) Comparison of initial nucleation barriers of bare Zn and ZNB@Zn electrodes. (b) GITT profiles of ZNB@Zn electrode at 1 mA cm^{-2} for 3 min and a rest of 3 min. (c) EIS evolutions of ZNB@Zn symmetric cell during cycling operated at 1 mA cm^{-2} for 1 mA h cm^{-2}. (d) Rate performances of bare Zn and ZNB@Zn symmetric cells. (e) Long-term galvanostatic charge/discharge cycles of symmetric cell at 1 mA cm^{-2}. (f) DOD of 34.1% at 10 mA cm^{-2} for 10 mA h cm^{-2}. (g) CE of bare Zn//bare Cu and ZNB@Zn//ZNB@Cu at 5 mA cm^{-2}. (h) Nb^- reconstruction of ZNB layer. Top 2D mapping and 3D reconstruction of ZnO^- and $ZnOH^-$ in cycled (i) bare Zn and (j) ZNB@Zn via TOF-SIMS. (k) $ZnOH^-$ depth profiles of two cycled anodes along with etching time.

time for over 1000 h at 10 mA cm^{-2} under 10 mA h cm^{-2}, exhibiting the high reversibility of the ZNB layer for Zn plating/stripping process. Furthermore, it is also evidenced by the CE of ZNB@Zn//ZNB@Cu asymmetric cell and it remained stable over 1200 cycles with a high average CE of 99.54%, whereas the bare Zn//Cu asymmetric cell experienced short circuit failure after only about 146 cycles (Fig. 4g and Fig. S16). Additionally, the precise measurement of CE for the Zn//Cu asymmetric cell using the pre-deposition-cycling method (Fig. S17) showed an improvement to 98.88% with the ZNB layer, compared to 97.92% for bare Zn, further justifying the reduction of Zn corrosion loss and excellent reversibility with ZNB layer [70–72].

Afterwards, the cycled Zn anode surfaces were analyzed via time-of-flight secondary-ion mass spectrometry (TOF-SIMS) to verify the plating morphology and species distribution (Fig. 4h). The 2D planar mapping and 3D reconstruction images clearly show (Fig. 4i and j) that compared to the uneven surface of bare Zn, the uniform distribution of ZnO^- further confirms the role of ZNB layer in guiding homogeneous Zn deposition. The 3D reconstruction of $ZnOH^-$ reveals that the protruded regions formed by dendrites on the bare Zn surface contain a large amount of hydrogen evolution by-products, while the cycled ZNB@Zn anode shows the smooth surface of the ZNB layer on the metallic Zn. The sputtering depth profile of $ZnOH^-$ shows same result of less side reaction product in the ZNB@Zn (Fig. 4k), demonstrating its protective effect on inhibiting corrosion reactions on the Zn anode surface.

The practical application of the ZNB@Zn anode was verified by assembling Zn//V_2O_{5-x} full cells [73]. As shown in Fig. 5(a), the cell employing ZNB@Zn exhibited lower polarization (131 and 61 mV) and resistance (Figs. S18 and S19). This improvement is attributed to the accelerated kinetics at the anode/electrolyte interface. Fig. 5 (b and c) and Fig. S20 show the rate performance of the cell based on ZNB@Zn anode and it provides specific capacity of 456 mA h g^{-1} at 0.2 A g^{-1}, retaining 361 mA h g^{-1} as the current increased to 10 A g^{-1}. In contrast, the specific capacity of full cell based on bare Zn dropped from 407 to 257 mA h g^{-1}, with notable capacity fluctuations under the operation of high current densities. Cycling at 1 A g^{-1} (Fig. 5d and e), the ZNB@Zn anode maintained a specific capacity of 393 mA h g^{-1} (90.2%) after 450 cycles, which is higher than that of bare Zn anode (332 mA h g^{-1}; 84.2%). At 5 A g^{-1}, the difference was enlarged and the ZNB@Zn full cell kept the capacity of 301 mA h g^{-1} after 3000 cycles with the CE of 99.99%, corresponding to the capacity retention rate of 80.21%. In contrast, the bare Zn-based full cell exhibited dramatic fluctuations in CE and failed at 2500 cycles with only 101 mA h g^{-1} (capacity retention of 30.49%). As displayed in Fig. S21, the ZNB@Zn full cell at a low current density of 0.5 A g^{-1} also kept great stability and reversibility, whereas the bare Zn full cell exhibited a rapid decline in capacity, indicating the effect of ZNB layer on fast desolvation and HER prohibition. The gradual increase in capacity of all the full cells at initial process under high current density is attributed to the activation process and the sufficient immersion of aqueous electrolyte. During this process, the wettability of the electrode/electrolyte interface at the high current density became much better, which helps to intercalate more Zn ions into the cathode interior. After resting of 24 h of period (Fig. 5f), ZNB@Zn-based full cell retained 97.86% of its initial capacity, while the bare Zn-based one retained only 82.64%, reflecting the protective effect of ZNB layer on preventing interface side reactions. To further validate the application potential of the ZNB coating, a large-size pouch cell was assembled.

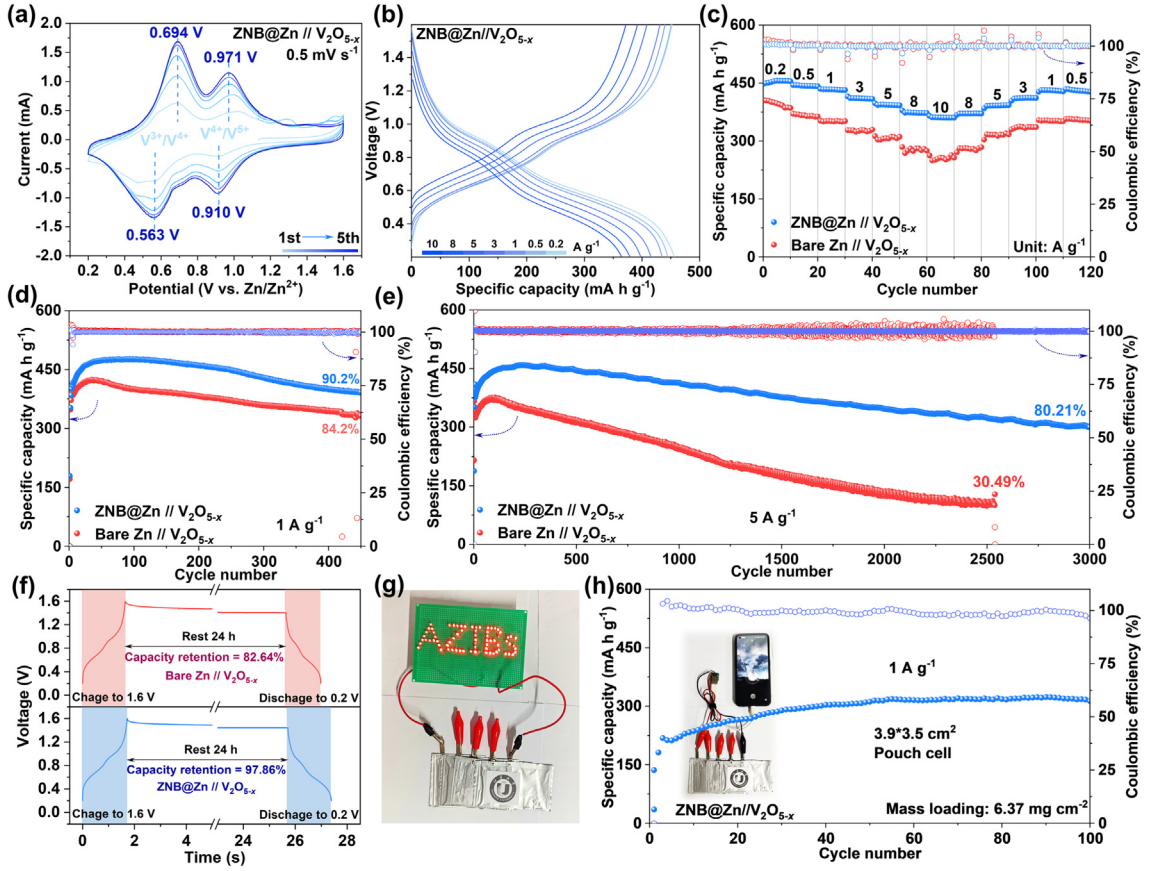

Fig. 5. (a) CV curve and (b) capacity-voltage curves of ZNB@Zn//V_2O_{5-x} full cell. Comparisons of (c) rate at up to 10 A g^{-1} and (d) cycling performance at 1 A g^{-1} of the full cells. (e) The long-term cycling performances of the full cells with/without ZNB at 5 A g^{-1}. (f) Self-discharge situation of full cell under resting for 24 h. (g) Digital photo and (h) cycling performance of large-areal ZNB@Zn//V_2O_{5-x} pouch cell at 1 A g^{-1}.

A high capacity of 322 mA h g^{-1} at 1 A g^{-1} was achieved with high cathode mass loading of 6.37 mg cm^{-2}, and it was stabilized for 100 cycles. Additionally, it successfully powered a series of light emitting diode (LED) light board or a smart phone after prolonged stable operation (Fig. 5g and h and Video S1), showcasing the promising prospects of the ZNB artificial interface layer for AZMBs.

4. Conclusions

In summary, the dielectric but ion-conductive ZNB layer is proposed on the metallic Zn surface, serving as an artificial SEI layer. The zincophilic properties and fast-ion-conducting channels of ZNB layer effectively facilitate the release of Zn^{2+} from the water-encased $Zn(H_2O)_6^{2+}$ solvation shell, promoting interfacial desolvation and transport kinetics across the SEI layer. As confirmed by SFG, Raman, electrochemical tests, as well as theoretical simulations, the crucial roles of ZNB layer in inducing rapid desolvation and diffusion have been explored, ensuring the fast and stable working of Zn anode, inducing dendrite-free deposition and protecting Zn anode from corrosion. As a consequence, ZNB@Zn electrode achieves a low overpotential of 24.9 mV, high average CE (99.54%), and long-term stable cycling for over 2000 h. The assembled ZNB@Zn-based full cell retains a capacity of 301 mA h g^{-1} after 3000 cycles at 5 A g^{-1} with a high-capacity retention rate of 80.21%. More importantly, the as-prepared large-areal pouch cell is also stabilized for hundreds of cycles and powers the smart devices, indicating the potential of the dielectric but ion-conductive layer in regulating ion transport kinetics for practical applications of AZMBs.

CRediT authorship contribution statement

Haifeng Yang: Writing – review & editing, Writing – original draft, Visualization, Validation, Software, Methodology, Investigation, Formal analysis, Data curation. **Jian Wang:** Writing – review & editing, Writing – original draft, Validation, Supervision, Resources, Project administration, Methodology, Funding acquisition, Conceptualization. **Panpan Zhang:** Software, Methodology, Funding acquisition, Data curation. **Xiaomin Cheng:** Validation, Data curation. **Qinghua Guan:** Validation, Data curation. **Jing Dong:** Validation, Data curation. **Bixian Chen:** Investigation, Data curation. **Lujie Jia:** Project administration. **Jing Zhang:** Validation, Data curation. **Yongzheng Zhang:** Investigation, Data curation. **Yunjian Liu:** Writing – review & editing, Supervision, Resources, Project administration, Methodology. **Hongzhen Lin:** Writing – review & editing, Supervision, Resources, Project administration, Funding acquisition, Formal analysis, Conceptualization.

Declaration of competing interest

The authors declare that they have no known competing financial interests or personal relationships that could have appeared to influence the work reported in this paper.

Acknowledgments

We acknowledge the National Key R&D Program of China (2021YFA1201503), the National Natural Science Foundation of China (21972164, 22279161, 12264038, 22309144), the Natural Science Foundation of Jiangsu Province (BK. 20210130), the China Postdoctoral Science Foundation (2023M733189), the Jiangsu Double-Innovation PhD Program in 2022 (JSSCBS20221241), the Senior Talents Fund of Jiangsu University (5501220014) as well as the technical support from Nano-X, Suzhou Institute of Nano-tech and Nano-bionics, Chinese Academy of Sciences. Dr. J. Wang thanks the fellowship funding provided by the Alexander von Humboldt Foundation. We are sincerely grateful to Dr. Jiqiang Jia from the Advanced Materials Analysis and Test Center of Xi'an University of Technology for the analysis and discussion of electronic microscopy..

The simulations were performed on resources and services provided by the National Computational Infrastructure (NCI) (project code: aj92), funded by the Australian Government, and the Pawsey Supercomputing Centre (project code: pawsey0990) which are supported by both the Australian Government and the Government of Western Australia.

Appendix A. Supplementary material

Supplementary data to this article can be found online at https://doi.org/10.1016/j.jechem.2024.09.010.

References

[1] J. Wang, H. Hu, S. Duan, Q. Xiao, J. Zhang, H. Liu, Q. Kang, L. Jia, J. Yang, W. Xu, H. Fei, S. Cheng, L. Li, M. Liu, H. Lin, Y. Zhang, Adv. Funct. Mater. 32 (2022) 2110468.
[2] M. Su, Y. Song, Q. Xu, H. Shi, Z. Wen, A. Dou, Y. Zhou, P. Zhang, Y. Liu, J. Energy Storage 95 (2024) 112585.
[3] M. Su, Y. Chen, Y. Song, A. Dou, J. Wang, G. Yan, Y. Zhou, Z. Wang, Y. Liu, Chem. Eng. J. 477 (2023) 147202.
[4] M. Su, M. Li, K. He, T. Wan, X. Chen, Y. Zhou, P. Zhang, A. Dou, H. Xu, C. Lu, R. Wang, D. Chu, Y. Liu, Chem. Eng. J. 455 (2023) 140802.
[5] Y. Wang, J. Xie, J. Luo, Y. Yu, X. Liu, X. Lu, Small Methods 6 (2022) 2200560.
[6] Y. Zhang, Z. Cao, S. Liu, Z. Du, Y. Cui, J. Gu, Y. Shi, B. Li, S. Yang, Adv. Energy Mater. 12 (2022) 2103979.
[7] T. Li, S. Yan, H. Dong, Y. Zheng, K. Ming, Y. Chen, H. Li, G. Li, Z. He, W. Li, Q. Wang, X. Song, J. Liu, E.H. Ang, Y. Wang, J. Energy Chem. 97 (2024) 1–11.
[8] Y. Zhu, J. Fan, S. Zhang, Z. Feng, C. Liu, R. Zhu, Y. Liu, P. Guan, M. Li, Z. Han, T. Wan, J. Tang, Q. Li, J. Yu, D. Chu, Chem. Eng. J. 480 (2024) 148334.
[9] Y. Shang, D. Kundu, Joule 7 (2023) 244–250.
[10] B. Li, X. Zhang, T. Wang, Z. He, B. Lu, S. Liang, J. Zhou, Nano-Micro Lett. 14 (2021) 6.
[11] B. Luo, Y. Wang, L. Sun, S. Zheng, G. Duan, Z. Bao, Z. Ye, J. Huang, J. Energy Chem. 77 (2023) 632–641.
[12] L. Yuan, J. Hao, C.C. Kao, C. Wu, H.K. Liu, S.X. Dou, S.Z. Qiao, L. Yuan, Energy Environ. Sci. 14 (2021) 5669–5689.
[13] X. Cheng, Y. Zuo, Y. Zhang, X. Zhao, L. Jia, J. Zhang, X. Li, Z. Wu, J. Wang, H. Lin, Adv. Sci. 11 (2024) 2401629.
[14] C. Li, X. Cheng, Y. Zhang, J. Zhu, H. Zhou, Y. Yang, J. Xu, J. Wang, Y. Wang, H. Yu, C. Shen, L. Zhan, L. Ling, J. Colloid Interface Sci. 671 (2024) 505–515.
[15] Z. Wu, Y. Zuo, Y. Zhang, X. Li, J. Zhang, Y. Wang, C. Shen, X. Cheng, M. Liu, H. Liu, H. Lin, J. Wang, L. Zhan, L. Ling, Energy Storage Mater. 70 (2024) 103463.
[16] J. Cao, D. Zhang, X. Zhang, Z. Zeng, J. Qin, Y. Huang, J. Cao, Energy Environ. Sci. 15 (2022) 499–528.
[17] Y. Gao, M. Wang, H. Wang, X. Li, Y. Chu, Z. Tang, Y. Feng, J. Wang, Y. Pan, Z. Ma, Z. Yang, D. Zhou, X. Li, J. Energy Chem. 84 (2023) 62–72.
[18] J. Liu, S. Hu, H. Guo, G. Zhang, W. Liu, J. Zhao, S. Song, C. Han, B. Li, J. Energy Chem. 95 (2024) 57–67.
[19] D. Xu, X. Ren, H. Li, Y. Zhou, S. Chai, Y. Chen, H. Li, L. Bai, Z. Chang, A. Pan, H. Zhou, Angew. Chem. Int. Ed. 63 (2024) e202402833.
[20] X. Wang, A. Naveed, T. Zeng, T. Wan, H. Zhang, Y. Zhou, A. Dou, M. Su, Y. Liu, D. Chu, Chem. Eng. J. 446 (2022) 137090.
[21] H. Bian, C. Wang, Y. Wang, Y. Ren, Y. Ge, H. Wu, B. Wang, D. Chen, B. Yang, D. Bin, Y. Li, J. Gu, Y. Ma, S. Tang, X. Meng, H. Lu, Adv. Funct. Mater. 34 (2024) 2401760.
[22] C. Guo, J. Zhou, Y. Chen, H. Zhuang, Q. Li, J. Li, X. Tian, Y. Zhang, X. Yao, Y. Chen, S. Li, Y. Lan, Angew. Chem. Int. Ed. 61 (2022) e202210871.
[23] X. Ye, X. Xiao, Z. Wu, X. Wu, L. Gu, S. Liu, J. Energy Chem. 97 (2024) 470–477.
[24] H. Yu, Y. Chen, W. Wei, X. Ji, L. Chen, ACS Nano. 16 (2022) 9736–9747.
[25] T. Li, X. Li, H. Yang, Y. Zhou, X. Li, M. Su, A. Dou, P. Zhang, X. Wu, A. Naveed, J. Sumner, Y. Liu, Materials Today Energy. 40 (2024) 101513.
[26] R. Zhao, J. Yang, X. Han, Y. Wang, Q. Ni, Z. Hu, C. Wu, Y. Bai, Adv. Energy Mater. 13 (2023) 2203542.
[27] W. Zhang, X. Zhu, L. Kang, Z. Peng, J. Zhu, L. Pan, L. Dai, S. Liu, L. Wang, Y. Liu, Z. He, J. Energy Chem. 90 (2024) 23–31.
[28] X. Li, P. Ye, A. Dou, Z. Jiang, A. Naveed, Y. Zhou, M. Su, P. Zhang, Y. Liu, J. Energy Storage. 76 (2024) 109874.
[29] B. Li, K. Yang, J. Ma, P. Shi, L. Chen, C. Chen, X. Hong, X. Cheng, M.-C. Tang, Y.-B. He, F. Kang, Angew. Chem. Int. Ed. 61 (2022) e202212587.
[30] L. Wang, W. Huang, W. Guo, Z.H. Guo, C. Chang, L. Gao, X. Pu, Adv. Funct. Mater. 32 (2022) 2108533.
[31] S. Wang, L. Hu, X. Li, D. Qiu, S. Qiu, Q. Zhou, W. Deng, X. Lu, Z. Yang, M. Qiu, Y. Yu, J. Energy Chem. 91 (2024) 203–212.

[32] H. Yu, Y. Chen, H. Wang, X. Ni, W. Wei, X. Ji, L. Chen, Nano Energy. 99 (2022) 107426.
[33] H. Yu, Q. Li, W. Liu, H. Wang, X. Ni, Q. Zhao, W. Wei, X. Ji, Y. Chen, L. Chen, J. Energy Chem. 73 (2022) 565–574.
[34] H. Yu, Z. He, D. Chen, P. Liu, H. He, L. Jiang, Y. Chen, L. Chen, Energy Reviews. (2024). https://doi.org/10.1016/j.enrev.2024.100107.
[35] L. Wang, B. Zhang, W. Zhou, Z. Zhao, X. Liu, R. Zhao, Z. Sun, H. Li, X. Wang, T. Zhang, H. Jin, W. Li, A. Elzatahry, Y. Hassan, H.J. Fan, D. Zhao, D. Chao, J. Am. Chem. Soc. 146 (2024) 6199–6208.
[36] S. Zhou, X. Meng, Y. Chen, J. Li, S. Lin, C. Han, X. Ji, Z. Chang, A. Pan, Angew. Chem. Int. Ed. 63 (2024) e202403050.
[37] J. Han, H. Euchner, M. Kuenzel, S.M. Hosseini, A. Groß, A. Varzi, S. Passerini, ACS Energy Lett. 6 (2021) 3063–3071.
[38] J. Wang, H. Hu, J. Zhang, L. Li, L. Jia, Q. Guan, H. Hu, H. Liu, Y. Jia, Q. Zhuang, S. Cheng, M. Huang, H. Lin, Energy Storage Mater. 52 (2022) 210–219.
[39] J. Wang, J. Zhang, S. Duan, L. Jia, Q. Xiao, H. Liu, H. Hu, S. Cheng, Z. Zhang, L. Li, W. Duan, Y. Zhang, H. Lin, Nano Lett. 22 (2022) 8008–8017.
[40] W. Li, D. Xu, P. Ruan, Y. Wan, X. Meng, Q. He, K. Liu, Y. Wang, S. Chai, Y. Song, Y. Xie, Z. Chang, A. Pan, Adv. Funct. Mater. (2024). https://doi.org/10.1002/adfm.202404146.
[41] D. Xu, Z. Wang, C. Liu, H. Li, F. Ouyang, B. Chen, W. Li, X. Ren, L. Bai, Z. Chang, A. Pan, H. Zhou, Adv. Mater. 36 (2024) 2403765.
[42] J. Wang, H. Hu, L. Jia, J. Zhang, Q. Zhuang, L. Li, Y. Zhang, D. Wang, Q. Guan, H. Hu, M. Liu, L. Zhan, H. Adenusi, S. Passerini, H. Lin, InfoMat. 6 (2024) e12558.
[43] X. Bi, N. Wu, C. Zhang, P. Bai, Z. Chai, X. Wang, Solid State Sci. 84 (2018) 86–94.
[44] Y.-N. Sun, C. Gao, L. Tao, G. Wang, D. Han, C. Li, H. Shan, Catal. Commun. 50 (2014) 73–77.
[45] Q. Peng, H. Liu, S. Ye, J. Electroanal. Chem. 800 (2017) 134–143.
[46] L. Yu, H. Liu, Y. Wang, N. Kuwata, M. Osawa, J. Kawamura, S. Ye, Angew. Chem. Int. Ed. 125 (2013) 5865–5868.
[47] X. Wei, X. Wen, Y. Liu, C. Chen, C. Xie, D. Wang, M. Qiu, N. He, P. Zhou, W. Chen, J. Cheng, H. Lin, J. Jia, X.Z. Fu, S. Wang, J. Am. Chem. Soc. 144 (2022) 11530–11535.
[48] J. Wang, J. Zhang, J. Wu, M. Huang, L. Jia, L. Li, Y. Zhang, H. Hu, F. Liu, Q. Guan, M. Liu, H. Adenusi, H. Lin, S. Passerini, Adv. Mater. 35 (2023) 2302828.
[49] J. Wang, J. Zhang, Y. Zhang, H. Li, P. Chen, C. You, M. Liu, H. Lin, S. Passerini, Adv. Mater. 36 (2024) 2402792.
[50] J. Zhang, R. He, Q. Zhuang, X. Ma, C. You, Q. Hao, L. Li, S. Cheng, L. Lei, B. Deng, X. Li, H. Lin, J. Wang, Adv. Sci. 9 (2022) 2202244.
[51] J. Wang, J. Zhang, S. Cheng, J. Yang, Y. Xi, X. Hou, Q. Xiao, H. Lin, Nano Lett. 21 (2021) 3245–3253.
[52] W.W. Rudolph, M.H. Brooker, P. Tremaine, Zeitschrift Für Physikalische Chemie. 209 (1999) 181–207.
[53] S. Chen, D. Ji, Q. Chen, J. Ma, S. Hou, J. Zhang, Nat. Commun. 14 (2023) 3526.
[54] P. Zhang, X. Wang, Y. Yang, H. Yang, C. Lu, M. Su, Y. Zhou, A. Dou, X. Li, X. Hou, Y. Liu, J. Colloid Interface Sci. 655 (2024) 383–393.
[55] P. Zhang, Y. Yang, X. Duan, Y. Liu, S. Wang, ACS Catal. 11 (2021) 11129–11159.
[56] G. Kresse, J. Furthmüller, Comput. Mater. Sci. 6 (1996) 15–50.
[57] G. Kresse, J. Furthmüller, Phys. Rev. B. 54 (1996) 11169–11186.
[58] J.P. Perdew, K. Burke, M. Ernzerhof, Phys. Rev. Lett. 77 (1996) 3865–3868.
[59] J. Liu, T.H. Wan, F. Ciucci, Electrochim. Acta. 357 (2020) 136864.
[60] F. Ciucci, C. Chen, Electrochim. Acta. 167 (2015) 439–454.
[61] M.B. Effat, F. Ciucci, Electrochim. Acta. 247 (2017) 1117–1129.
[62] T.H. Wan, M. Saccoccio, C. Chen, F. Ciucci, Electrochim. Acta. 184 (2015) 483–499.
[63] Y. Lu, C.Z. Zhao, J.Q. Huang, Q. Zhang, Joule. 6 (2022) 1172–1198.
[64] S.-M. Lee, J. Kim, J. Moon, K.N. Jung, J.H. Kim, G.J. Park, J.-H. Choi, D.Y. Rhee, J.-S. Kim, J.W. Lee, M.-S. Park, Nat. Commun. 12 (2021) 39.
[65] Y. Zhang, W. Zhao, C. Kang, S. Geng, J. Zhu, X. Xiao, Y. Ma, H. Huo, P. Zuo, S. Lou, G. Yin, Matter. 6 (2023) 1928–1944.
[66] M. Yan, C. Xu, Y. Sun, H. Pan, H. Li, Nano Energy. 82 (2021) 105739.
[67] L. Yao, J. Liu, F. Zhang, B. Wen, X. Chi, Y. Liu, Nat. Commun. 15 (2024) 6249.
[68] Y. Wang, L.e. Mo, X. Zhang, Y. Ren, T. Wei, Y. He, Y. Huang, H. Zhang, P. Tan, Z. Li, J. Zhou, L. Hu, Adv. Energy Mater. 14 (2024) 2402041.
[69] Z. Xiang, Y. Qiu, X. Guo, K. Qi, Z.L. Xu, B.Y. Xia, Energy Environ. Sci. 17 (2024) 3409–3418.
[70] B.D. Adams, J. Zheng, X. Ren, W. Xu, J.-G. Zhang, Adv. Energy Mater. 8 (2018) 1702097.
[71] A. Mohammadi, S. Djafer, S. Sayegh, A.J. Naylor, M. Bechelany, R. Younesi, L. Monconduit, L. Stievano, Chem. Mater. 35 (2023) 2381–2393.
[72] J. Xiao, Q. Li, Y. Bi, M. Cai, B. Dunn, T. Glossmann, J. Liu, T. Osaka, R. Sugiura, B. Wu, J. Yang, J.G. Zhang, M.S. Whittingham, Nat. Energy. 5 (2020) 561–568.
[73] X. Dou, X. Xie, S. Liang, G. Fang, Science Bulletin. 69 (2024) 833–845.